

A STUDY OF OUTFLOWS IN LUMINOUS QUASARS AT REDSHIFT $\sim 0.4 - 0.8$

J. WANG,^{1,2} D. W. XU,^{1,2} AND J. Y. WEI^{1,2}

¹Key Laboratory of Space Astronomy and Technology, National Astronomical Observatories, Chinese Academy of Sciences, Beijing 100012, China

²School of Astronomy and Space Science, University of Chinese Academy of Sciences, Beijing, China

(Received July 1, 2016; Revised September 27, 2016; Accepted November 28, 2017)

Submitted to ApJ

ABSTRACT

We perform a systematic study of outflow in the narrow-line region (NLR) of active galactic nuclei (AGNs) at $z \sim 0.4 - 0.8$ basing upon a large sample of ~ 900 quasars at $z \sim 0.4 - 0.8$. The sample is extracted from the Sloan Digital Sky Survey by mainly requiring 1) the g-band magnitude is brighter than 19 magnitude; and 2) the [O III] $\lambda 5007$ emission line has a signal-to-noise ratio larger than 30. Profiles of multiple emission lines are modeled by a sum of several Gaussian functions. The spectral analysis allows us to identify 1) a prevalence of both [O III] $\lambda 5007$ line blue asymmetry and bulk velocity blueshift of both [Ne III] $\lambda 3869$ and [Ne III] $\lambda 3426$ lines, when the [O II] $\lambda 3727$ line is used as a reference. The velocity offset of [O III] $\lambda 5007$ line is, however, distributed around zero value, except for a few outliers. 2) not only the significant [O III] $\lambda 5007$ line asymmetry, but also the large bulk velocity offsets of [Ne III] $\lambda 3869$ and [Ne V] $\lambda 3426$ emission lines tend to occur in the objects with high L/L_{Edd} , which is considerably consistent with the conclusions based on local AGNs. With three M_{BH} estimation methods, the significance level of the trend is found to be better than 2.9σ , 3.2σ and 1.8σ for [O III], [Ne III] and [Ne V], respectively. After excluding the role of radio jets, the revealed dependence of NLR gas outflow on L/L_{Edd} allows us to argue that the pressure caused by the wind/radiation launched/emitted from central supermassive black hole is the most likely origin of the outflow in these distant quasars, which implies that the outflow in luminous AGNs up to $z \sim 1$ have the same origin.

Keywords: galaxies: nuclei — quasars: emission lines — galaxies: active

arXiv:1711.09775v1 [astro-ph.GA] 24 Nov 2017

1. INTRODUCTION

A widely accepted idea on the growth of supermassive black holes (SMBHs) is the co-evolution of SMBHs and their host galaxies where the SMBHs reside in (see a recent review in Heckman & Best 2014). In the idea, a feedback process is generally necessary to self-regulate SMBH growth and star formation in the host galaxy by either sweeping out circumnuclear gas in both galaxy merger and secular evolution scenarios (e.g., Alexander & Hickox 2012; Kormendy & Ho 2013; Villar-Martin et al. 2016; Woo et al. 2017) or triggering star formation by compressing the gas (e.g., Zubovas et al. 2013; Ishibashi & Fabian 2014). For instance, a suppressed star formation is revealed in high- z ($z = 1 \sim 3$) powerful active galactic nuclei (AGNs) basing upon the Herschel SPIRE observations in sub-millimeter (Page et al. 2012). On the contrary, a positive feedback is revealed in the observations of individual objects (e.g., Cresci et al. 2015; Carniani et al. 2016)

As suggested by both semianalytic models and numerical simulations, the feedback process is required not only to reproduce the observed $M_{\text{BH}} - \sigma_*$ relation, luminosity functions of quasars, and normal galaxies (e.g., Haehnelt et al. 1998; Silk & Rees 1998; Fabian 1999; Kauffmann & Haehnelt 2000; Granato et al. 2004; Di Matteo et al. 2005, 2007; Springel et al. 2005; Croton et al. 2006; Hopkins et al. 2007, 2008; Khalatyan et al. 2008; Menci et al. 2008; Somerville et al. 2008), but also to solve the “over cooling” problem in the Λ cold dark matter (Λ CDM) galaxy formation model in which the cooling predicted in galaxy groups and clusters is stronger than the observed one (e.g., Ciotti & Ostriker 2007; Somerville et al. 2008, Hirschmann et al. 2014). Dehnen & King (2013) proposed a scenario of SMBH growth in which the SMBH accretion disk is formed because the gas that is swept-up by the feedback finally falls towards the SMBH on near-parabolic orbit when the feedback weakens.

The occurrence of feedback from central SMBH can be diagnosed by the frequently observed outflows on various scales (see reviews in Veilleux et al. 2005 and Fabian 2012). The outflows can be traced by the blueshifted absorption lines in optical, UV, and soft-X-ray spectra (e.g., Crenshaw et al. 2003; Hamann & Sabra 2004; Wang & Xu 2015 and references therein). In addition, it can be more conveniently traced by the blue asymmetry of strong [O III] $\lambda\lambda$ 4959, 5007 doublet and its bulk blueshift with respect to the local system (e.g., Heckman et al. 1981; Veron-Cetty et al. 2001; Zamanov et al. 2002; Marziani et al. 2003; Aoki et al. 2005; Bian et al. 2005; Boroson 2005; Komossa et al. 2008; Xu & Komossa 2009; Mullaney et al. 2013; Zhang et al. 2013; Harrison et al. 2014).

The origin of both blue asymmetry of the [O III] doublet and its bulk blueshift has been largely examined in past decades. However, discrepant conclusions have been drawn for AGNs at local universe. Three kinds of modes, including AGN wind (e.g., Crenshaw et al. 2003; Pounds et al. 2003; Ganguly et al. 2007; Reeves et al. 2009; Dunn et al. 2010; Tombesi et al. 2012), radiation pressure (e.g., Granato et al. 2004; Alexander et al. 2010), and mechanical energy outflow caused by a collimated radio jet (e.g., Best et al. 2006; Holt et al. 2008; Nesvadba et al. 2008; Rosario et al. 2010; Guillard et al. 2012), are proposed for a driving of the observed asymmetry and bulk blueshift. On the one hand, ample studies indicate that strong blue asymmetry and large the bulk velocity blueshift (especially the extreme “blue outliers” defined as the objects with [O III] bulk blueshift larger than 250km s^{-1} , Zamanov et al. 2002) tend to occur in the AGNs with high Eddington ratio (L/L_{Edd} , where $L_{\text{Edd}} = 1.26 \times 10^{38}(M_{\text{BH}}/M_{\odot}) \text{ erg s}^{-1}$ is the Eddington luminosity) (e.g., Bian et al. 2005; Boroson 2005; Zhang et al. 2011; Wang et al. 2011, 2016; Wang 2015; Zamanov et al. 2002; Zhou et al. 2006; Komossa et al. 2008). A coevolution between the outflow traced by [O III] λ 5007 line and host galaxy has been revealed by Wang et al. (2011) and Wang (2015) for both local type I and II AGNs. The authors argued that the coevolution is most likely driven by the coevolution of L/L_{Edd} . On the other hand, a dependence of the [O III] line width on radio luminosity at 1.4 GHz ($L_{1.4\text{GHz}}$) has been reported for a sample of flat-spectrum radio galaxies (e.g., Heckman et al. 1984; Whittle 1985). This result was confirmed and reinforced by Mullaney et al. (2013) and Zakamska & Greene (2014) for a large sample of both local type I and type II AGNs detected by the SDSS spectroscopic survey.

Feedback from AGN is expected to be strong in high redshift AGNs where the peaks of both AGN’s activity and star formation occur roughly coincident (e.g., Ishibashi et al., 2013). Extremely energetic outflows with a kinetic energy flux of $\sim 1 - 5\%L_{\text{bol}}$ have been identified in four high- z luminous QSOs by using UV absorption lines as a tracer of outflow (e.g., Borguet et al. 2013; Arav et al. 2013 and references therein). With the spatially resolved maps of the kinematics of the ionized gas, galactic-scale outflows have been identified in a number of radio-quiet and extremely radio-loud AGNs at $z \sim 1 - 3$ (e.g., Alexander et al. 2010; Nesvadba et al. 2006, 2008). The outflow at high redshift of $z = 6.4189$ was revealed by Maiolino et al. (2012) in SDSS J114816.64+525150.3 by a detection of the broad wing of the [C II] λ 158 μm emission.

Even though the comprehensive studies have been carried out for the outflows of local AGNs, the outflows at early universe have been so far only focused on a number of objects with unusual properties. In this paper, we perform a systematic study on the outflow of ~ 900 AGNs at intermediate redshift $z \sim 0.4 - 0.8$, which is the largest sample at this redshift range so far, by focusing on their gas kinematics diagnosed by highly-ionized narrow emission lines.

The paper is organized as follows. The sample selection and spectral analysis are presented in Sections 2 and 3, respectively. The analysis and statistical results are shown in Section 4, and the implications are discussed in Section 5. A Λ CDM cosmology with parameters $H_0 = 70 \text{ km s}^{-1}\text{Mpc}^{-1}$, $\Omega_m = 0.3$, and $\Omega_\Lambda = 0.7$ (Spergel et al. 2003) is adopted throughout the paper.

2. SAMPLE SELECTION

We start from the Sloan Digital Sky Survey Data Release 7 (SDSS DR7) catalog (Abazajian et al. 2009). After focusing on the objects classified as QSOs (i.e., *spclass* = 3) by the SDSS pipelines (Bromley et al. 1998; Glazebrook et al. 1998), we require the objects have 1) a redshift between 0.4 and 0.8. This requirement is used to ensure both [O III] λ 5007 and Mg II λ 2800 emission lines can be covered by the SDSS spectroscopic wavelength range; 2) a *g*-band magnitude brighter than 19 magnitude, which is necessary for a proper modeling of the optical continuum. To model the emission line profile reliable, we further require the [O III] λ 5007 emission line has $S/N > 30$. The uncertainty of the emission line σ_l is estimated from $\sigma_l = \sigma_c N^{1/2} [1 + \text{EW}/(N\Delta)]^{1/2}$ (e.g., Perez-Montero & Diaz 2003), where σ_c is the standard deviation of the continuum in a box near the line, N is the number of pixels used to integrate line flux, EW is the equivalent width of the line, and Δ is the wavelength dispersion in unit of \AA pixel^{-1} .

With these selections, there are finally in total 981 entries in our sample.

3. SPECTRAL MODELING

The 1-Dimensional spectra of these AGNs are analyzed by the IRAF¹ package. At the beginning, each spectrum is corrected for the Galactic extinction basing upon the color excess $E(B - V)$ taken from the Schlegel, Finkbeiner, and Davies Galactic reddening map (Schlegel et al. 1998). An $R_V = 3.1$ extinction law (Cardelli et al., 1989) of the MilkyWay is adopted in the correction. Each extinction-corrected spectrum is then shifted to the rest frame, along with the flux correction due to the relativity effect, by using the redshift provided by the SDSS pipelines.

3.1. Continuum Modeling and Removal

The continuum of each rest-frame spectrum is modeled by a linear combination of three components: (1) a broken power law from the central AGN, in which the wavelength of the break point and the two spectral indices are not fixed in the continuum modeling, (2) a template of both high-order Balmer emission lines and a Balmer continuum from the broad-line region (BLR), and (3) an empirical template of both optical and ultraviolet Fe II complex. The intrinsic extinction due to the host galaxy is involved in the modeling by a galactic extinction curve with $R_V = 3.1$. A χ^2 minimization is iteratively performed over the whole SDSS spectroscopic wavelength range in the observe-frame, which roughly corresponds to a rest-frame wavelength range from 2700 to 6500 \AA , except for the regions with known emission lines (e.g., H β , H γ , H δ , [O III] λ 4959, 5007, [O II] λ 3727, [Ne III] λ 3869, [Ne V] λ 3426, and Mg II λ 2800). The modeling and removal of the continuum is illustrated in the left panels of Figure 1 for two typical cases, one with weak optical Fe II complex, and the another with strong Fe II complex.

The case B recombination model with an electron temperature of $T_e = 1.5 \times 10^4\text{K}$ and an electron density of $n_e = 10^{8-10} \text{ cm}^{-3}$ (Storey & Hummer 1995) is adopted as the used template of the high-order Balmer lines (i.e., H $_7$ -H $_{50}$). The line width of the high-order Balmer lines is fixed to be that of the broad component of H β , which is determined by our line profile modeling (see below). The Balmer continuum f_λ^{BC} is approximately modeled by the emission from a partially optically thick cloud by following Dietrich et al. (2002), see also in Grandi (1982) and Malkan & Sargent (1982):

$$f_\lambda^{\text{BC}} = f_\lambda^{\text{BE}} B_\lambda(T_e)(1 - e^{-\tau_\lambda}); \lambda \leq \lambda_{\text{BE}} \quad (1)$$

where f_λ^{BE} is the continuum flux at the Balmer edge $\lambda_{\text{BE}} = 3464\text{\AA}$, and $B_\lambda(T_e)$ is the Planck function at an electron temperature of $T_e = 1.0 \times 10^4\text{K}$. τ_λ is the optical depth at wavelength λ , which is related to the one at the Balmer edge τ_{BE} as $\tau_\lambda = \tau_{\text{BE}}(\lambda/\lambda_{\text{BE}})^3$. We adopt a typical value of $\tau_{\text{BE}} = 0.5$ in the current Balmer continuum fitting.

¹ IRAF is distributed by National Optical Astronomy Observatory, which is operated by the Association of Universities for Research in Astronomy, Inc., under cooperative agreement with the National Science Foundation.

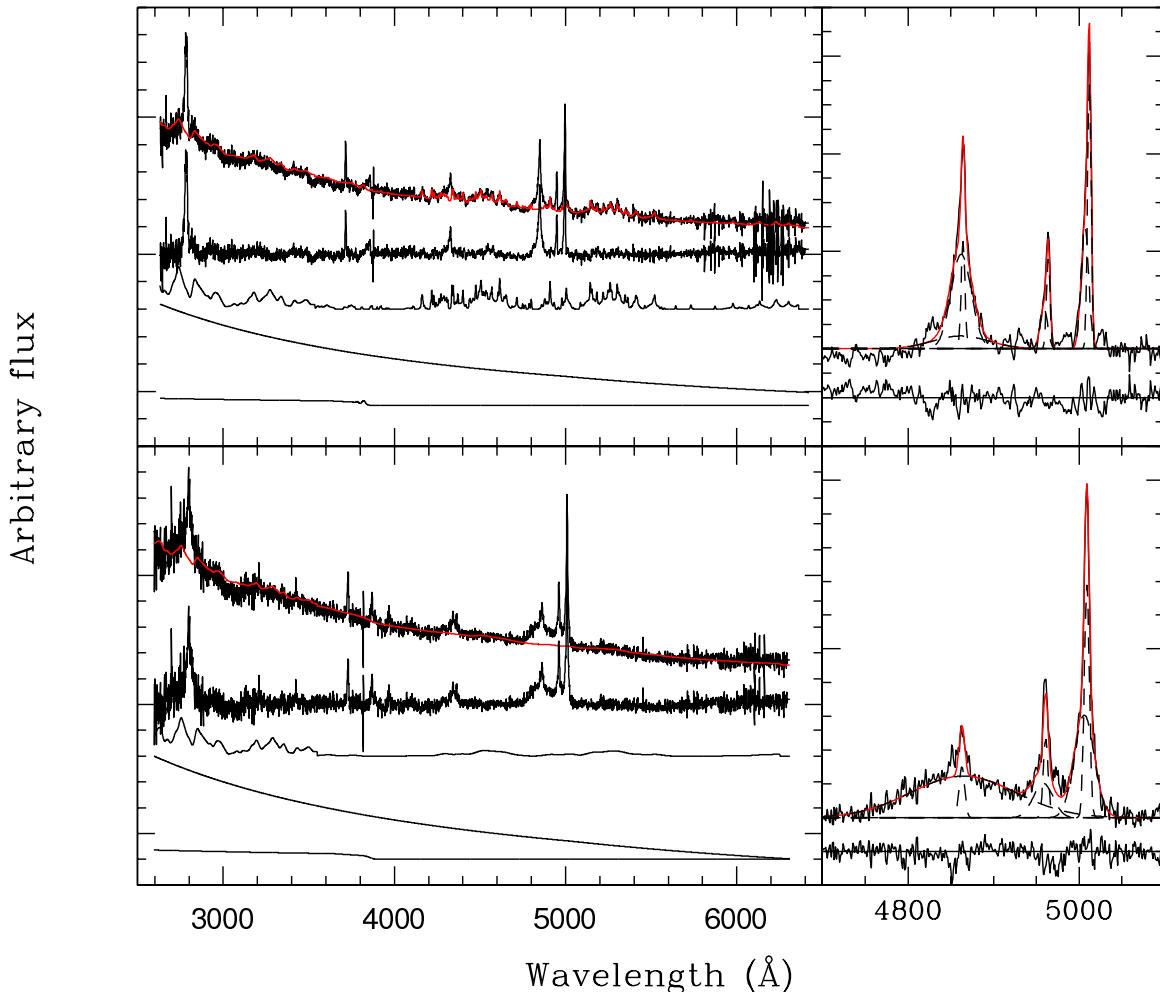


Figure 1. *Left panels:* Illustration of the modeling and removal of the continuum for two typical cases. In each panel, the top curve shows the observed rest-frame spectrum overplotted by the modeled continuum by the red curve. The continuum-removed emission-line spectrum is shown below the observed one. The modeled continuum is obtained by a reddened linear combination of the emission from both optical and UV Fe II complex, a broken power law from the central AGN, the Balmer continuum, and the high-order Balmer emission lines, which are plotted in ordinates below the emission-line spectrum. The intrinsic extinction is considered in the modeling by using a galactic extinction curve with $R_V = 3.1$. All of the spectra are shifted vertically by an arbitrary amount for visibility. *Right panels:* Line profile modelings by a linear combination of a set of Gaussian functions for the $H\beta$ region, in which the modeled continuum has already been removed from the original observed spectrum. The observed and modeled line profiles are plotted by black and red solid lines, respectively. Each Gaussian function is shown by a dashed line. The sub-panel underneath the line spectrum presents the residuals between the observed and modeled profiles.

The optical and ultraviolet Fe II complex in each rest-frame spectrum are modeled by the empirical templates provided in Veron-Cetty et al. (2004) and by the theoretical template in Bruhweiler & Verner (2008), respectively. For the optical template, both the broad and narrow components of the Fe II emission are included in the modeling. The line widths of the broad and narrow Fe II emission are determined from the line profile modeling of the $H\beta$ emission line (see below). Bruhweiler & Verner (2008) calculated a grid of ultraviolet Fe II emission spectra. The predicted spectrum giving the best fit to the observed IZW 1 spectrum is adopted in the current study, which is calculated for $\log[n_{\text{H}}/(\text{cm}^{-3})] = 11.0$, $\log[\Phi_{\text{H}}/(\text{cm}^{-2} \text{s}^{-1})] = 20.5$, $\xi/(1 \text{ km s}^{-1}) = 20$, and 830 energy levels. Again, the template is broadened by convolution with a Gaussian profile having the same width as the $H\beta$ broad emission.

3.2. Emission Line Profile Modeling

3.2.1. $H\beta$ and $[O \text{ III}]\lambda 5007$

After the removal of the continuum, we model the emission-line profiles of $H\beta$ and $[O\ III]\lambda\lambda 4959, 5007$ of each spectrum by a linear combination of a set of several Gaussian profiles through the SPECIFY task (Kriss 1994) in the IRAF packages. Generally speaking, a linear combination of two or three Gaussian profiles are required to reproduce the observed $[O\ III]\lambda\lambda 4959, 5007$ line profiles well in most of the cases. In addition, a linear combination of two or three broad Gaussian functions is necessary for adequately reproducing the observed broad Balmer line profile in about a half of the sample. In each of these cases, a residual $H\beta$ line profile, which is obtained by subtracting the modeled narrow-line component (including the modeled forbidden lines) from the observed profile, is then used to measure the line width and integrated line flux of the broad $H\beta$ emission. In the modelings, the line flux ratio of the $[O\ III]$ doublet is fixed to its theoretical value. The line width of the narrow $H\beta$ component is fixed to equal that of the $[O\ III]$ core line, if the resulted two widths are significantly different. In order to properly model the $[O\ III]\lambda 5007$ line profile, a broad He $I\lambda 5016$ emission line (Veron et al. 2002) is additionally required in the line profile modelings in a few objects. The line modelings are schematically presented in the right panels of Figure 1 for the $H\beta$ and $[O\ III]\lambda\lambda 4959, 5007$ emission lines.

3.2.2. Other Emission Lines

With the similar technique, a combination of a single Gaussian profile and a local linear pseudo-continuum is adopted to model $[O\ II]\lambda 3727$, $[Ne\ III]\lambda 3869$ and $[Ne\ V]\lambda 3426$ forbidden lines through a χ^2 minimization. The level of the pseudo-continuum is determined by both red and blue emission just outside individual emission line, which accounts for the residual resulted from our continuum removal aforementioned in Section 3.1, because the three forbidden lines are typically relatively weak in the spectra.

In summary, our spectral analysis of the $H\beta$ region is available for 884 quasars at redshift between 0.4 and 0.8, except for three objects whose $H\beta$ emission is too weak to be modeled. There are in total 782 objects whose $[O\ II]\lambda 3727$ line emission has $S/N > 5$. With the same criterion, the total entries of available measurements of $[Ne\ III]\lambda 3869$ and $[Ne\ V]\lambda 3426$ are 570 and 329, respectively.

4. ANALYSIS AND RESULTS

4.1. $[O\ III]\lambda 5007$ Line Asymmetry

By modeling the $[O\ III]\lambda 5007$ emission-line profile by a sum of several Gaussian profiles, we follow Wang et al. (2016) to parametrize the asymmetry of the $[O\ III]$ line by a velocity of δv , defined as

$$\delta v = \frac{\sum_{k=1}^n f_k (v_k - v_p)}{\sum_{k=1}^n f_k} \quad (2)$$

where f_k and v_k is the modeled flux and velocity of the k th Gaussian function, respectively. v_p denotes the velocity of the Gaussian profile that reproduces the peak of the observed line profile. A negative value of δv corresponds to a blue asymmetry, and a positive one corresponds to a red asymmetry. Wang et al. (2016) has shown that the asymmetry parameter defined in Equation (2) is related with the parameter defined in Harrison et al. (2014) quite well, which quantifies the line asymmetry by comparing the measured line widths/centers (in units of either wavelength or velocity) at different line flux levels (e.g, Heckman et al. 1981; Whittle 1985; Veilleux 1991; Wang et al. 2011; Liu et al. 2013), even through there is a small systematical difference between the two definitions.

4.2. Bulk Velocity Shifts of Forbidden Lines

We calculate bulk relative velocity shifts of high-ionized emission lines (i.e., $[O\ III]\lambda 5007$, $[Ne\ III]\lambda 3869$, and $[N\ V]\lambda 3426$) with respect to the $[O\ II]\lambda 3727$ emission line. The $[O\ II]$ emission line is adopted as a velocity shift reference in the current study for two reasons. At first, although the narrow $H\beta$ emission line is widely used as a reference in a great deal of previous studies, recent studies indicate that the narrow Balmer lines show an evident velocity shift relative to the galaxy rest frame. Hu et al. (2008) suggested that the $[O\ II]$ emission line might be a more reliable reference than either $[O\ III]$ or $H\beta$ in local type I AGNs. In a large sample of $\sim 23,000$ local type II AGNs, Bae & Woo (2014) found that $H\alpha$ shows large velocity offsets being comparable to that of $[O\ III]$ in $\sim 3\%$ of the sample when the host galaxy is adopted as a reference. A large velocity shift of $\sim 200\text{ km s}^{-1}$ in the host-galaxy frame is

identified for both narrow H α and H β lines in SDSS J112611.63+425246.4, a Balmer-absorption AGN, by Wang & Xu (2015). Secondly, the poor H β profile prohibits an available extraction of the H β narrow component in $\sim 20\%$ objects listed in our sample.

The finally used bulk relative velocity shift is defined as $\Delta v = c\Delta\lambda/\lambda_0$, where λ_0 and $\Delta\lambda$ are the rest-frame wavelength in vacuum of a given emission line and the wavelength shift of the line with respect to the [O II] $\lambda 3727$ emission line, respectively. $\Delta\lambda$ is obtained from the modeled line centers as $\Delta\lambda = (\lambda^{\text{ob}} - \lambda_{[\text{OII}]}^{\text{ob}}) - (\lambda_0 - \lambda_{0,[\text{OII}]})$, where λ^{ob} ($\lambda_{[\text{OII}]}^{\text{ob}}$) and λ_0 ($\lambda_{0,[\text{OII}]}$) are the observed line center resulted from our profile modeling and the line wavelength in vacuum of a given ([O II]) line, respectively. A negative value of Δv corresponds to a blueshift, and a positive value corresponds to a redshift.

4.3. Velocity Dispersion of Broad H β Emission Line

We measure the velocity dispersion of the broad H β component $\sigma_{\text{H}\beta}$ of each object from the H β broad line profile obtained by subtracting the modeled narrow-line component. The dispersion is based on the definition given in Peterson et al. (2004):

$$\sigma_{\text{H}\beta}^2 = \frac{\int \lambda^2 f_{\lambda} d\lambda}{\int f_{\lambda} d\lambda} - \bar{\lambda}^2 \quad (3)$$

where f_{λ} is the line specific flux after a subtraction of the continuum and $\bar{\lambda} = \int \lambda f_{\lambda} d\lambda / \int f_{\lambda} d\lambda$ is the first moment of the line profile.

4.4. Estimation of M_{BH} and L/L_{Edd}

Both SMBH mass (M_{BH}) and L/L_{Edd} are the critical parameters describing AGN phenomena (e.g., Shen & Ho 2014). The great progress made in the reverberation mapping technique (e.g., Kaspi et al. 2000, 2005; Peterson & Bentz 2006; and see Marziani & Sulentic 2012 and Peterson 2014 for recent reviews; Wang et al. 2014; Du et al. 2015) allows us to estimate M_{BH} (and also L/L_{Edd}) basing upon the broad emission line in a single epoch spectroscopy (e.g., Wu et al. 2004).

M_{BH} is estimated from the modeled broad H β line emission for all the 884 intermediate- z quasars, except for the three objects without available H β profile modeling, according to several calibrated relationships.

At first, the estimation of M_{BH} provided in Vestergaard & Peterson (2006, and references therein) is given as

$$M_{\text{BH}} = 10^{6.67} \left(\frac{L_{\text{H}\beta}}{10^{42} \text{ erg s}^{-1}} \right)^{0.63} \left(\frac{\text{FWHM}(\text{H}\beta)}{1000 \text{ km s}^{-1}} \right)^2 M_{\odot} \quad (4)$$

where $L_{\text{H}\beta}$ is the luminosity of the H β broad component and $\text{FWHM}(\text{H}\beta)$ is the line width of broad H β emission that is resulted from our line profile modeling (Section 3.2.1). Secondly, an alternative M_{BH} estimation based on the line dispersion $\sigma_{\text{H}\beta}$ is obtained through the method presented in Collin et al. (2006) who argued that the M_{BH} estimated from line dispersion is less biased than that from FWHM. Finally, we obtain an additional M_{BH} estimation in which the impact of radiation pressure on the kinematics of BLR gas is taken into account of by following the calibration reported in Marconi et al. (2008)

$$\frac{M_{\text{BH}}}{M_{\odot}} = \tilde{f} \left(\frac{\text{FWHM}(\text{H}\beta)}{1000 \text{ km s}^{-1}} \right)^2 \left(\frac{L_{5100}}{10^{44} \text{ erg s}^{-1}} \right)^{0.5} + g \left(\frac{L_{5100}}{10^{44} \text{ erg s}^{-1}} \right) \quad (5)$$

where the logarithmic of the two parameters \tilde{f} and g are $6.13_{-0.30}^{+0.15}$ and $7.72_{-0.05}^{+0.06}$, respectively. L_{5100} is the AGN's continuum luminosity at 5100Å that is inferred from H β line luminosity through the calibration given in Greene & Ho (2005)

$$L_{5100} = 7.31 \times 10^{43} \left(\frac{L_{\text{H}\beta}}{10^{42} \text{ erg s}^{-1}} \right)^{0.883} \text{ erg s}^{-1} \quad (6)$$

In order to obtain $L_{\text{bol}}/L_{\text{Edd}}$, the bolometric luminosity L_{bol} of each object is estimated from the usually used bolometric correction $L_{\text{bol}} = 9\lambda L_{\lambda}(5100\text{\AA})$ (Kaspi et al. 2000). Note that, in the above estimations the intrinsic extinction is not applied for $L_{\text{H}\beta}$ because the Balmer decrement that is traditionally used is either unavailable or unreliable for most of the objects.

Table 1. Correlations coefficient matrix related with outflow velocities measured from the forbidden emission lines.

Property	$\delta v([\text{O III}])$	$\Delta v([\text{O III}])$	$\Delta v([\text{Ne III}])$	$\Delta v([\text{Ne V}])$
	(1)	(2)	(3)	(4)
(1) FWHM($\text{H}\beta$)	0.184($< 10^{-4}$)	0.179($< 10^{-4}$)	0.223($< 10^{-4}$)	0.218($< 10^{-4}$)
(2) $L/L_{\text{Edd}}(\text{V06})$	-0.183($< 10^{-4}$)	-0.198($< 10^{-4}$)	-0.249($< 10^{-4}$)	-0.288($< 10^{-4}$)
(3) $L/L_{\text{Edd}}(\text{C06})$	-0.122($< 10^{-4}$)	-0.177($< 10^{-4}$)	-0.205($< 10^{-4}$)	-0.165($< 10^{-4}$)
(4) $L/L_{\text{Edd}}(\text{M08})$	-0.173($< 10^{-4}$)	-0.203($< 10^{-4}$)	-0.261($< 10^{-4}$)	-0.233($< 10^{-4}$)

4.5. Statistical Results

With the quantification of line asymmetry, bulk velocity offset, M_{BH} and L/L_{Edd} , the main statistical results are presented in this subsection.

4.5.1. Outflow and SMBH Accretion

FWHM($\text{H}\beta$) versus outflow. The top line in Figure 2 plots the line width of $\text{H}\beta$ broad emission as a function of [O III] line asymmetry δv , bulk velocity offsets Δv of [O III], [Ne III] and [Ne V] from left to right. The left panel in the top line shows that 1) blue asymmetry is quite prevalent for the [O III] emission line, which is consistent with previous results concluded from the samples of local type I and II AGN’s (e.g., Harrison et al. 2014; Mullaney et al. 2013; Wang et al. 2011, 2016); and 2) stronger the blue asymmetry, smaller the FWHM($\text{H}\beta$) (i.e., $\text{FWHM}(\text{H}\beta) < 5000 \text{ km s}^{-1}$) will be. One can see from the FWHM($\text{H}\beta$) versus $\Delta v_{[\text{OIII}]}$ plot that the bulk velocity offset of [O III] line is almost asymmetrically distributed around zero value², except for a few outliers with extremely large bulk blueshift. The outliers typically have small $\text{FWHM}(\text{H}\beta) < 5000 \text{ km s}^{-1}$, which agrees with previous studies on local AGNs in quality. The local extreme “blue outliers”, usually defined as the objects with [O III] bulk blueshift larger than 250 km s^{-1} , are found to dominantly occur in the AGNs with small $\text{FWHM}(\text{H}\beta)$ (e.g., Zamanov et al. 2002; Zhou et al. 2006; Komossa et al. 2008). Not as similar as the case of $\Delta v_{[\text{OIII}]}$, both [Ne III] and [Ne V] emission lines show a dominance of bulk velocity blueshift whose value decreases with $\text{FWHM}(\text{H}\beta)$.

$\text{H}\beta$ Line profile versus outflow. The panels in the second line of Figure 2 is the same as the top one, but for $\text{FWHM}/\sigma_{\text{H}\beta}$ that depends on the line profile caused by a variety of line-of-sight kinematics and/or inclination of BLR gas. We theoretically have $\text{FWHM}/\sigma_{\text{H}\beta} = 2\sqrt{2\ln 2} = 2.35$ for a pure Gaussian profile, and $\rightarrow 0$ for a pure Lorentzian profile. The four panels in the line show that the measured outflow velocities are independent on the $\text{FWHM}/\sigma_{\text{H}\beta}$, i.e., kinematics and/or inclination of BLR, although there seems to be a weak tendency for the case of [Ne V] in which large velocity offset tends to occur in the objects with stronger line wings (i.e., $\text{FWHM}/\sigma_{\text{H}\beta} \sim 1.5$).

L/L_{Edd} versus outflow. The L/L_{Edd} based on the three M_{BH} estimations are plotted against the measured outflow velocities in the panels from lines 3 to 5 in Figure 2. A comparison of the three estimations of L/L_{Edd} allows us to draw a robust conclusion: Aside from the bulk velocity offset of [O III], objects with stronger [O III] line blue asymmetry, larger bulk blueshift of both [Ne III] and [Ne V] emission lines tend to be associated with higher L/L_{Edd} , although an object with large L/L_{Edd} does not necessarily have strong [O III] line blue asymmetry and large bulk blueshift possibly due to the orientation of the outflow. Finally, we emphasize that no dependence can be found when L/L_{Edd} is taken place by either $\text{H}\beta$ (and [O III]) luminosity or M_{BH} .

Table 1 lists the corresponding correlation coefficient matrix that is obtained from the Spearman rank-order test. For each correlation coefficient, the corresponding probability of the null correlation is shown in the bracket. We emphasize that the weak correlation significance shown in the table has no essential impact on the conclusion of this study. Our conclusion states that a high L/L_{Edd} is a necessary, rather than a sufficient, condition for significant outflow, because the measured outflow velocity additionally depends on the orientation of the outflow with respect to the line-of-sight of an observer.

² In fact, when the host galaxy is used as a reference, Wang & Xu (2016) revealed a marginal bulk blueshift of [O III] emission line of $-10 \pm 30 \text{ km s}^{-1}$ in a case study of Balmer-absorption AGN SDSS J112611.63+425246.4

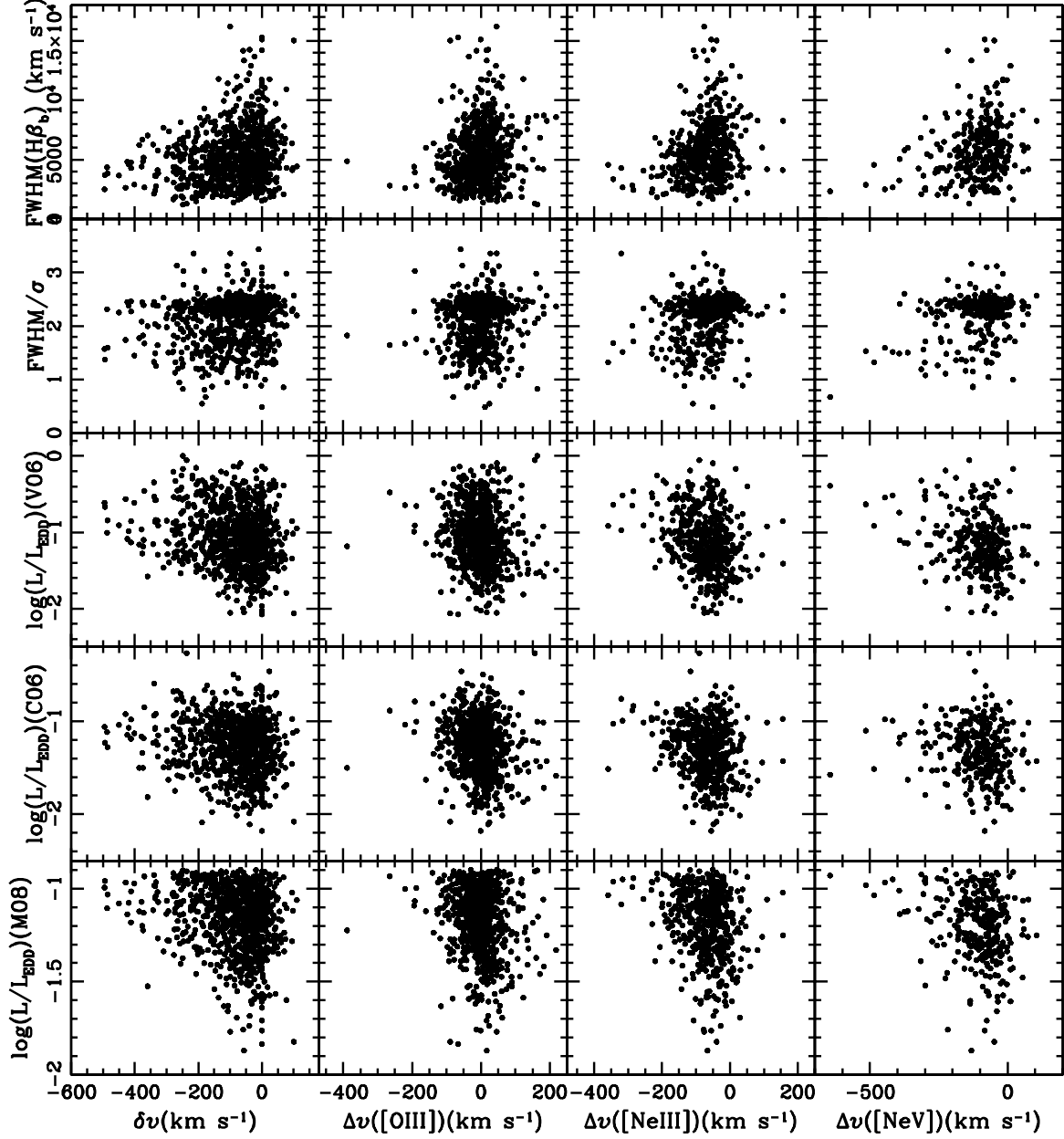


Figure 2. *Line 1:* from left to right, line width of H β broad emission (FWHM) is plotted as a function of [O III] λ 5007 line asymmetry δv defined in Equation (2), bulk velocity shift Δv of [O III] λ 5007, [Ne III] λ 3869 and [Ne V] λ 3426 emission lines. All the Δv are determined by using [O II] λ 3727 line as a reference. A positive velocity denotes a redshift, and a negative value a blueshift. *Line 2:* the same as line 1, but for FWHM/ $\sigma_{H\beta}$, where $\sigma_{H\beta}$ is estimated based on the definition in Eq. (3). *Lines 3-5:* the same as line 1, but for the L/L_{Edd} estimated through three calibrations, see Section 4.4 for the details.

As an additional test, we separate the entire sample into two parts basing upon the measured line profile asymmetry and bulk velocity shifts, i.e., $\delta v([\text{OIII}]) = -150 \text{ km s}^{-1}$, $\Delta v([\text{NeIII}]) = -150 \text{ km s}^{-1}$ and $\Delta v([\text{NeV}]) = -200 \text{ km s}^{-1}$. Figure 3 compares the normalized distributions of L/L_{Edd} estimated from the three methods between the two parts. For each of the panels, a two-sided Kolmogorov-Smirnov test is performed to check whether the high-velocity and low-velocity parts are drawn from the sample population. The results of the Kolmogorov-Smirnov tests are listed in Table 2. Each entry contains the probability that the two samples are drawn from the same parent population, along with the maximum absolute discrepancy.

The statistical tests indicate that, for the $\delta v([\text{OIII}])$ case, we can reject the hypothesis that the two L/L_{Edd} distributions are drawn from the same parent population at a significance level better than 3σ (assuming a Gaussian

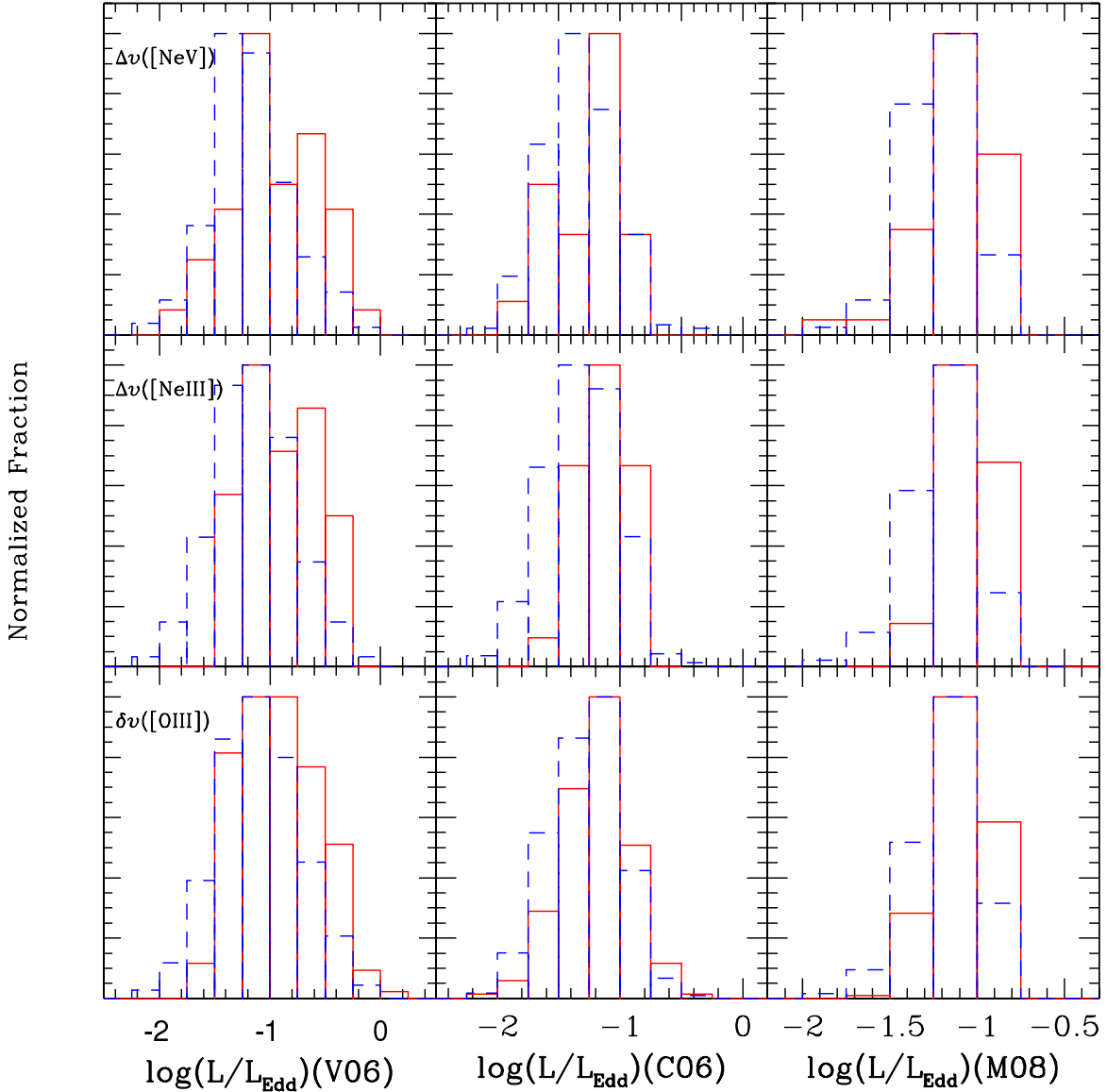


Figure 3. Comparisons of the normalized distributions of the L/L_{Edd} between the high-velocity and low-velocity groups. The panels at the bottom are for $\delta v([\text{O III}])$ for the L/L_{Edd} estimated from the three different methods (see Section 4.4 for the details.). The middle and top panels are the same as the bottom ones, but for $\Delta v(\text{Ne III})$ and $\Delta v(\text{Ne V})$, respectively. In each panel, the red-solid and blue-dashed lines denote high-velocity and low-velocity groups, respectively. The two groups are separated at a velocity of -150 km s^{-1} for $\delta v([\text{O III}])$ and $\Delta v(\text{Ne III})$, and at a velocity of -200 km s^{-1} for $\Delta v(\text{Ne V})$.

function) when the M_{BH} is estimated from Vestergaard & Peterson (2006) and Marconi et al. (2008), although the significance level decreases to 2.9σ when the method in Collin et al. (2006) is adopted. A similar trend could be found in the $\Delta v([\text{NeV}])$ case, in which the method in Collin et al. (2006) results in the lowest significance level of 1.8σ . On the contrary, in the $\Delta v([\text{NeIII}])$ case, the same hypothesis can be rejected at a significance level better than 3σ for all the three M_{BH} estimation methods, in which the best result (3.7σ) is obtained when the method in Collin et al. (2006) is adopted.

4.5.2. L/L_{Edd} vs. δv : [OIII] Luminosity on kpc Scale or Outflow

We obtained a dependence of L/L_{Edd} on the [O III] line asymmetry measured by the parameter δv defined in Eq. (2) in Section 4.5.1. One would argue that a large asymmetry is caused by a faint [O III] emission from the narrow emission-line region (NLR) on kpc scale with a kinematics under the gravitation of the host galaxy rather than a strong emission from outflow gas. Additional test is therefore performed to test the potential impact of this effect as

Table 2. Two-sided Kolmogorov-Smirnov Test Matrix.

Property	δv ([O III])	Δv ([Ne III])	Δv ([Ne V])
	(1)	(2)	(3)
(1) L/L_{Edd} (V06)	8.1×10^{-5} (0.19)	1.3×10^{-3} (0.28)	4.7×10^{-3} (0.29)
(2) L/L_{Edd} (C06)	4.1×10^{-3} (0.15)	2.0×10^{-4} (0.32)	6.9×10^{-2} (0.22)
(3) L/L_{Edd} (M08)	2.2×10^{-5} (0.20)	8.5×10^{-4} (0.29)	2.9×10^{-3} (0.30)

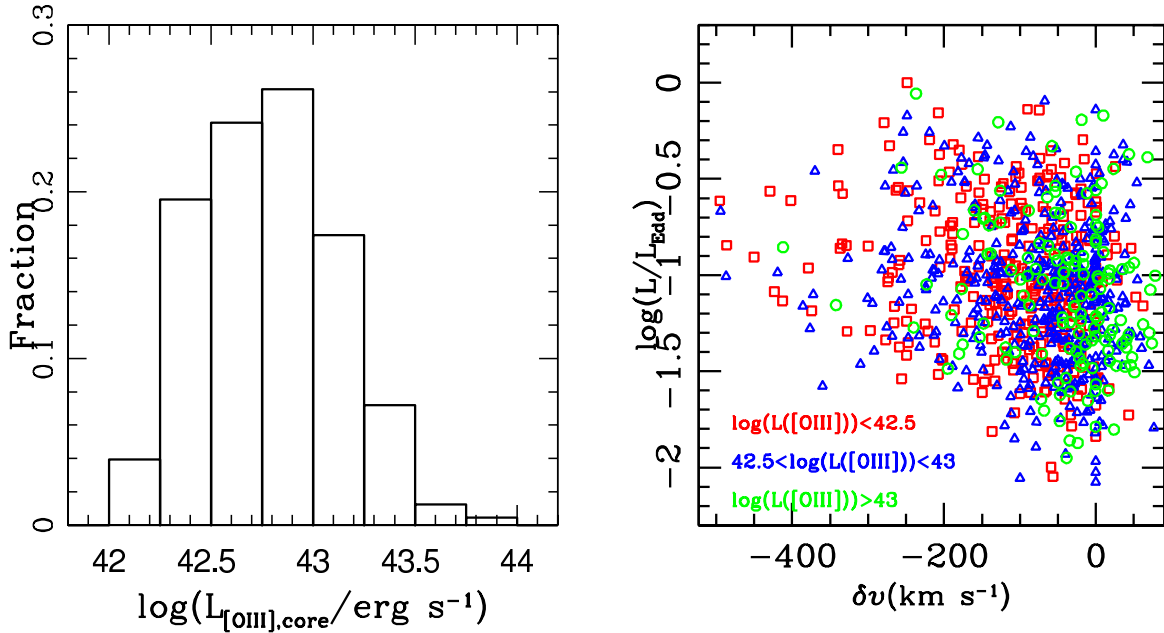


Figure 4. *Left panel:* Distribution of the [O III] λ 5007 line luminosity from NLR at kpc scale, which is obtained in Section 4.5.2. *Right panel:* L/L_{Edd} versus δv diagram, in which the total sample is separated into three groups according to their NLR [O III] line luminosities. The three groups are over-plotted in the same diagram by different colors and symbols.

follows. At the beginning, since most of the objects show a blue [O III] asymmetry, we obtain the [O III] luminosity of NLR in kpc scale $L_{[\text{OIII}],\text{NLR}}$ of each object through a scale³ $L_{[\text{OIII}],\text{NLR}} = 2L_{[\text{OIII}],\text{red}}$, where $L_{[\text{OIII}],\text{red}}$ is the line luminosity redward of the line peak, although we admit that this procedure potentially yields an over-estimation of the $L_{[\text{OIII}],\text{NLR}}$. The left panel in Figure 4 presents the distribution of $L_{[\text{OIII}],\text{NLR}}$.

With the distribution, the total sample is then separated into three groups according to their $L_{[\text{OIII}],\text{NLR}}$: Group 1 has $\log L_{[\text{OIII}],\text{NLR}} < 42.5$, Group 2 has $42.5 \leq \log L_{[\text{OIII}],\text{NLR}} < 43.0$ and Group 3 has $\log L_{[\text{OIII}],\text{NLR}} \geq 43.0$. All the three groups are over-plotted in the L/L_{Edd} vs. δv diagram in the right panel of Figure 4. A comparison of the distributions on the diagram suggests a consistence for all the three groups, which indicates that our conclusion on the L/L_{Edd} vs. δv dependence is indeed resulted from a change of outflow luminosity rather than a change of NLR luminosity in kpc scale. A two-dimensional Kolmogorov-Smirnov test (Peacock 1983; Fasano & Franceschini 1987) yields a significance level of $< 4.5 \times 10^{-3}$ for the hypothesis that the three groups are from different populations.

4.5.3. NLR Stratification

The AGN’s NLR gas has been generally believed to be stratified in density and ionization potential for a long time (e.g., Filippenko & Halpern 1984; Filippenko 1985; De Robertis & Osterbrock 1986). A systematic stratification of kinematics of NLR gas is illustrated in Figure 5 for the studied $z \sim 0.4 - 0.8$ quasars, which compares the bulk velocity

³ We do not use the modeled narrow core component given by the spectral profile modeling described in Section 3.2.1, because based on our experience the modeled core component is quite unreliable in the case with a smooth, significant blue line wing, even though the total profile and flux can be modeled quite well with multiple Gaussian components.

offset with the ionization potential (IP) for three different emission lines: more highly ionized emission line tends to be associated with larger bulk blueshift, which is consistent with previous studies (e.g., Komossa et al. 2008; Wang & Xu 2016). The red squares and errorbars in the plot represents the average value and the corresponding standard deviation at a confidence level of 1σ , which yields a best-fit relation of $\Delta v = (106.6 \pm 152.9) - (2.3 \pm 2.3)IP$.

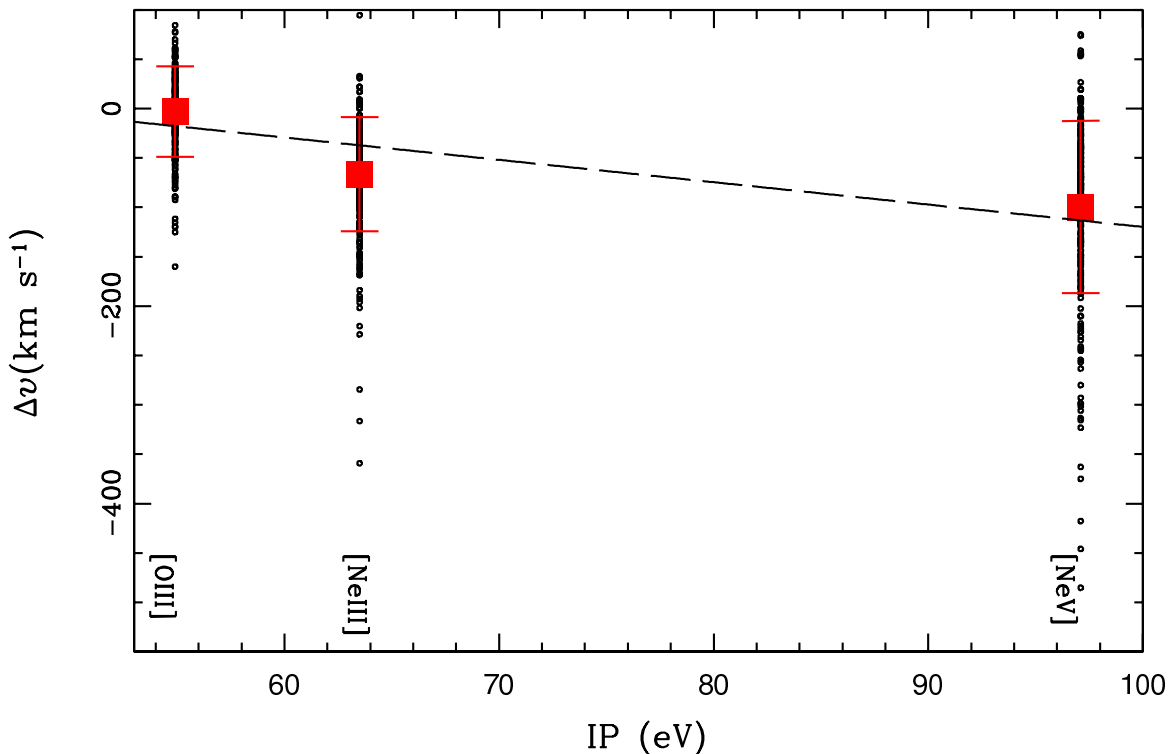


Figure 5. An illustration of kinematic stratification of NLR gas by plotting the determined bulk velocity shift (Δv) against ionization potential (IP) for [O III] λ 5007, [Ne III] λ 3869 and [Ne V] λ 3426 emission lines. The small dots represent the measurements of individual objects listed in our sample. The red squares and the corresponding uncertainties are the mean values and corresponding 1σ standard deviations. The best-fit line is overlotted by the dashed line.

5. DISCUSSION

5.1. Disk Wind/Radiation Origin of Outflow

We identify a dependence of L/L_{Edd} on both blue wing of [O III] λ 5007 line and bulk blueshift of high-ionized [Ne III] λ 3869 and [Ne V] λ 3426 for quasars at $z \sim 0.4 - 0.8$, which allows us to argue that L/L_{Edd} is the physical driver of the outflows occurring in the narrow-line region of AGNs up to $z \sim 1$. The role of L/L_{Edd} on outflow has been, in fact, frequently revealed in nearby AGNs. Basing upon the large SDSS spectroscopic survey, a dependence of L/L_{Edd} on both [O III] asymmetry and bulk blueshift has been identified in local luminous AGNs. Generally speaking, stronger the blue asymmetry and larger the bulk velocity blueshift, higher the L/L_{Edd} will be (e.g., Bian et al. 2005; Boroson 2005; Zhang et al. 2011; Wang et al. 2011; Wang 2015). Matsuoka (2012) shows a deficit of the extended emission-line region in the AGNs with high L/L_{Edd} , which could be explained either by the AGN's outflow that blows the gas around central SMBH away or by galaxy minor merger. Wang et al. (2016) recently identified a direct dependence of [O III] blue asymmetry on the accretion process occurring around the central SMBH by a joint X-ray and optical spectral analysis: stronger [O III] blue asymmetry tends to occur in local AGNs with both steeper hard-X-ray spectra and higher L/L_{Edd} .

In the theoretical ground, the outflow from luminous AGNs is proposed to be explained by the wind/radiation model. In the model, the observed outflow is caused by the wind/radiation pressure launched/emitted from the inner accretion disk (e.g., Murray et al. 1995; Proga et al. 2000; Crenshaw et al. 2003; King & Pounds 2003; Pounds et al. 2003; King 2003, 2005; Ganguly et al. 2007; Reeves et al. 2009; Alexander et al. 2010; Dunn et al. 2010; King

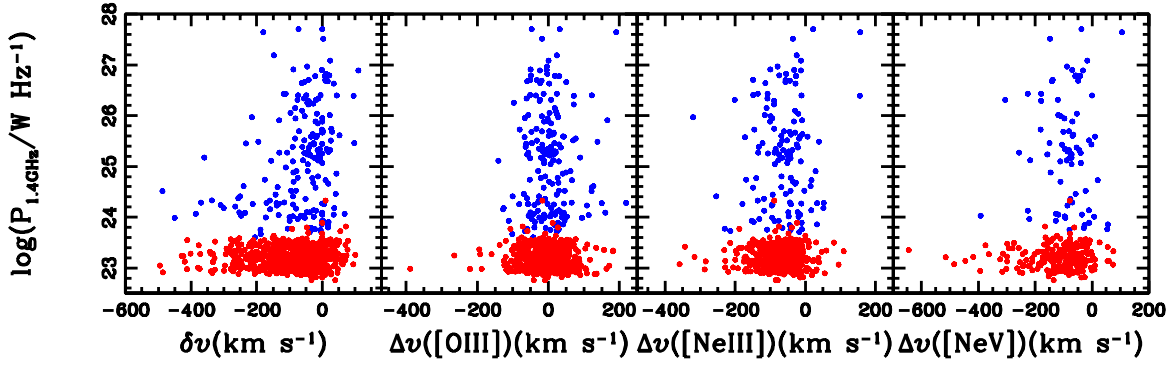


Figure 6. The same as in Figure 2 but for 1.4GHz radio power at rest-frame. The sources with a detected radio flux are shown by the blue points, and the ones with a flux upper limit by the red points.

et al. 2011; Zubovas & King 2012; Fabian 2012). The disk wind model has been successfully applied to explain the observed broad ultraviolet absorption lines in a fraction of $\sim 20\%$ quasars and the ultrafast outflows identified from the blueshifted X-ray Fe XXV and Fe XXVI absorptions in a few local AGNs (e.g., Tombesi et al. 2012; Higginbottom et al. 2014). The hydrodynamic outflow model calculated by Proga et al. (2008) indicates that the wind launched from the accretion disk can extend into the inner NLR, though the specific launch mechanism is still under debate. Possible mechanisms include radiation/line-driven (e.g., Proga et al. 1998, 2000; Laor & Brandt 2002; Proga & Kallman 2004; Nomura et al. 2013; Higginbottom et al. 2014; Hagino et al. 2015), thermally driven (e.g., Begelman et al. 1983; Krolik & Kriss 2001), magnetically driven (e.g., Blandford & Payne 1982; Ferreira 1997; Fukumura et al. 2014; Stepanovs & Fendt 2014), and hybrid models (e.g., Proga 2003; Everett 2005).

5.2. Radio Emission

In addition to the wind/radiation model, another major scenario of outflow is that the outflow in NLR is driven by the interaction between the radio jet and the interstellar medium (e.g., Heckman et al. 1984; Whittle 1985; Brotherton 1996; Whittle & Wilson 2004; Morganti et al. 2007; Holt et al. 2008, 2011; Nesvadba et al. 2008; Guillard et al. 2012; Mahony et al. 2013; Mullaney et al. 2013; Zakamska & Greene 2014).

To examine the role of radio emission, we follow Wang et al. (2016) by cross-matching the ~ 900 quasars at $z \sim 0.4 - 0.8$ with the FIRST survey catalog (Becker et al. 2003). The cross-match with a radius of $3''$ returns 183 objects with detected radio emission exceeding the FIRST limiting flux density (5σ) of 1mJy. The radio power at 1.4 GHz (rest frame) of each detection is obtained from the observed integrated flux density at 1.4 GHz f_ν through $P_{1.4\text{GHz}} = 4\pi d_L^2 f_\nu (1+z)^{-1-\alpha}$, where d_L is the luminosity distance, and $\alpha = -0.8$ (e.g., Ker et al. 2012) is the spectral slope defined as $f_\nu \propto \nu^{-\alpha}$. For each of the objects without a detection, an upper limit of radio power is inferred from the reported detection limit at the corresponding celestial position through the same transformation.

The calculated $P_{1.4\text{GHz}}$ is plotted as a function of [O III] line asymmetry, bulk velocity offsets of [O III], [Ne III] and [Ne V] emission lines in Figure 6. In each panel, the blue points denote the sources with a detected radio flux, and the red points the ones with a flux upper limit. One can see from the figure that in the current sample both strength of the [O III] blue wing and bulk velocity blueshifts of [Ne III] and [Ne V] are unlikely driven by radio emission. This independence therefore allows us to exclude the radio jet origin of outflow in the current sample. In fact, the objects with strong [O III] blue asymmetry or large bulk velocity offsets instead tend to have either less or undetected radio power.

5.3. Comparison to Local AGNs

In this subsection, the quantified [O III] line asymmetry based on the current sample is compared to that of nearby X-ray selected type-I AGNs studied in Wang et al. (2016), simply because both studies adopt the same definition of line asymmetry quantification. In the following comparison, we ignore the possible systematics in L/L_{Edd} estimations caused by different calibrations: the L/L_{Edd} is estimated by extinction-corrected H α broad emission in Wang et al. (2016) and by H β in the current study. In fact, the effect on L/L_{Edd} due to extinction correction is quite small because L/L_{Edd} is scaled to line luminosity as $L/L_{\text{Edd}} \sim L_{\text{H}\alpha, \text{H}\beta}^{1/4}$.

The comparison between the two samples is illustrated in Figure 7. The lower two panels compare the cumulative distributions of $L_{H\beta}$ and M_{BH} . One can clearly see that, when compared to the sample of local AGNs, the quasar sample investigated in the current study is strongly biased towards the objects with high luminosity and large SMBH mass end. This significant discrepancy can be naturally explained by the detection limit effect in which only bright enough sources can be detected at higher redshift for a given flux limit.

The top-left and top-right panels compare the cumulative distributions of the quantified asymmetry and estimated L/L_{Edd} between the two samples, respectively. As shown by the comparisons, the local AGN sample is biased towards both stronger asymmetry and higher L/L_{Edd} . A two-side 1-dimensional Kolmogorov-Smirnov test shows a significant difference between the two samples. The mean values of δv are -84 ± 3 and -97 ± 15 km s $^{-1}$ for the intermediate- z quasars and nearby X-ray-selected AGNs, respectively. The corresponding mean values of L/L_{Edd} are 0.25 ± 0.03 and 0.13 ± 0.01 . This difference is not hard to be understood since the local AGNs in Wang et al. (2016) are X-ray selected, which biased against less active objects. The X-ray luminosities in an energy band from 2 to 10 keV of these local X-ray selected AGNs range from 10^{42} to 10^{44} erg s $^{-1}$, and the L/L_{Edd} from 0.01 to 1. In fact, bright local AGNs usually have a L/L_{Edd} with a range of at least 3 orders of magnitude from 0.001 to 1 (e.g., Woo & Urry 2002; Boroson 2002). Basing upon the 2-10 keV X-ray luminosity, the L/L_{Edd} of the Palomar optically selected AGNs ranges from 10^{-5} to 0.1 (Panessa et al. 2006).

Even though this difference, the intermediate- z quasars studied in this paper are combined with the local X-ray selected AGNs studied in Wang et al. (2016) in Figure 8. The figure plots L/L_{Edd} against [O III] $\lambda 5007$ line asymmetry, which indicates that the local X-ray-selected AGNs are consistent with the $z \sim 0.4 - 0.8$ quasars in terms of the L/L_{Edd} distribution as a function of the [O III] $\lambda 5007$ line asymmetry. A two-dimensional Kolmogorov-Smirnov test again yields a probability of 1.7×10^{-5} that the two samples are drawn from the different parent populations.

6. CONCLUSIONS

The outflow is systematically examined for a large sample of ~ 900 quasars at $z \sim 0.4 - 0.8$ selected from SDSS in this paper. By modeling profiles of multiple emission lines by a sum of several Gaussian functions, we identify a prevalence of not only [O III] $\lambda 5007$ line blue asymmetry, but also bulk velocity blueshift of both [Ne III] $\lambda 3869$ and [Ne III] $\lambda 3426$ lines, which are tend to be associated with a high L/L_{Edd} . These results allow us to argue that the pressure caused by the wind/radiation launched/emitted from central SMBH is the most likely origin of the outflow in these distant quasars, which further implies that the outflow in luminous AGNs up to $z \sim 1$ have the same origin.

The authors would like to thank the anonymous referee for his/her very useful comments and suggestions for improving the manuscript. The study is supported by the National Natural Science Foundation of China under grants 11473036 and 11773036, This study uses the SDSS archive data that was created and distributed by the Alfred P. Sloan Foundation.

REFERENCES

- Abazajian, K. N., Adelman-McCarthy, J. K., Agueros, M. A., et al. 2009, ApJS, 182, 543
- Alexander, D. M., & Hickox, R. C. 2012, NewAR, 56 ,93
- Alexander, D. M., Swinbank, A. M., Smail, Ian, McDermid, R., & Nesvadba, N. P. H. 2010, MNRAS, 402, 2211
- Aoki, K., Kawaguchi, T., & Ohta, K. 2005, ApJ, 618, 601
- Arav, N., Borguet, B., Chamberlain, C., Edmonds, D., & Danforth, C. 2013, MNRAS, 436, 3286
- Bae, Hyun-Jin, & Woo, Jong-Hak. 2014, ApJ, 795, 30
- Becker, R. H., Helfand, D. J., White, R. L., Gregg, M. D., & Laurent-Muehleisen, S. A. 2003, VizieR Online Data Catalog 807
- Begelman, M. C., McKee, C. F., & Shields, G. A. 1983, ApJ, 271, 70
- Best, P. N., Kaiser, C. R., Heckman, T. M., & Kauffmann, G. 2006, MNRAS, 368, 67
- Blandford, R. D., & Payne, D. G. 1982, MNRAS, 199, 883
- Bian, W. H., Yuan, Q. R., & Zhao, Y. H. 2005, MNRAS, 364, 187
- Borguet, B. C. J., Arav, N., Edmonds, D., Chamberlain, C., & Benn, C. 2013, ApJ, 762, 49
- Boroson, T. A. 2002, ApJ, 565, 78
- Boroson, T. A. 2005, AJ, 130, 381
- Bromley, B. C., Press, W. H., Lin, H., & Kirshner, R. P. 1998, ApJ, 505, 25
- Bruhweiler, F., & Verner, E. 2008, ApJ, 675, 83
- Brotherton, M. S. 1996, ApJS, 102, 1

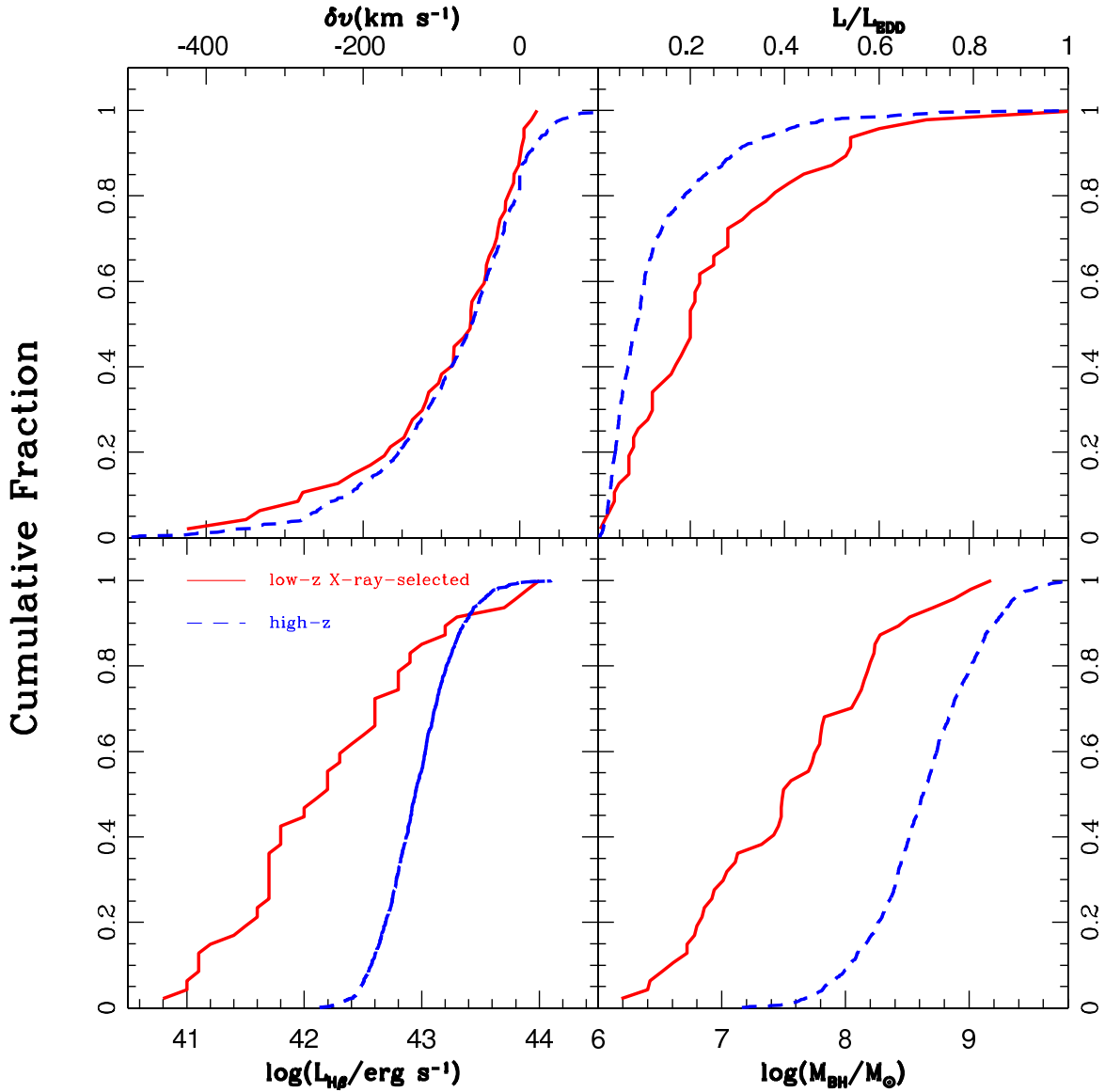


Figure 7. Comparisons between the $z \sim 0.4 - 0.8$ quasars of this study and the local X-ray-selected AGNs studied in Wang et al. (2016). The cumulative distributions of the $z \sim 0.4 - 0.8$ quasars are shown by blue dashed lines, and those of local X-ray-selected AGNs by the red solid lines.

Cardelli, J. A., Clayton, G. C., & Mathis, J. S. 1989, *ApJ*, 345, 245

Carniani, S., Marconi, A., Maiolino, R., et al. 2016, *A&A*, 591, A28

Ciotti, L., & Ostriker, J. P. 2007, 665, 1038

Collin, S., Kawaguchi, T., Peterson, B. M., & Vestergaard, M. 2006, *A&A*, 456, 75

Crenshaw, D. M., et al. 2003, *ApJ*, 594, 116

Cresci, G., Marconi, A., Zibetti, S., et al. 2015, *A&A*, 582, A63

De Robertis, M. M., & Osterbrock, D. E. 1986, *ApJ*, 301, 727

Dietrich, M., Hamann, F., Shields, J. C., Constantin, A., Vestergaard, M., Chaffee, F., Foltz, C. B., & Junkkarinen, V. T. 2002, *ApJ*, 581, 912

Di Matteo, P., Combes, F., Melchior, A.-L., & Semelin, B. 2007, *A&A*, 468, 61

Di Matteo, T., Springel, V., & Hernquist, L. 2005, *Nature*, 433, 604

Du, P., Wang, J. M., Hu, C., Valls-Gabaud, D., Baldwin, J. A., Ge, J. Q., & Xue, S. J. 2014, *MNRAS*, 438, 2828

Dunn, J. P., et al. 2010, *ApJ*, 709, 611

Everett, J. E. 2005, *ApJ*, 631, 689

Fabian, A. C. 1999, *MNRAS*, 308, L39

Fabian, A. C. 2012, *ARA&A*, 50, 455

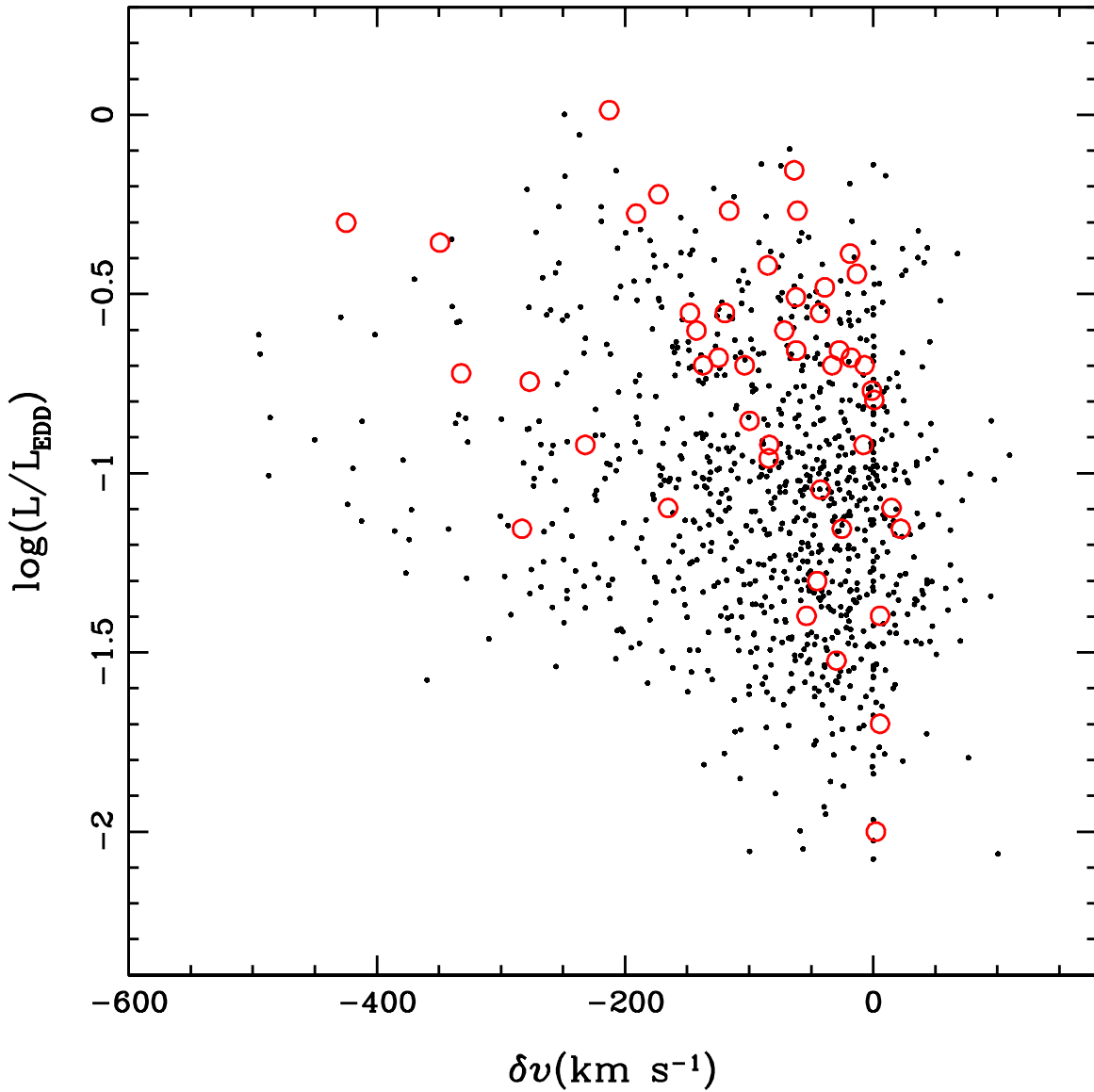


Figure 8. [O III] λ 5007 emission line asymmetry δv plotted against L/L_{Edd} . The black points denote the measurements of the $z \sim 0.4 - 0.8$ quasars obtained in this study, and the red open circles the measurements of the local X-ray-selected AGNs studied in Wang et al. (2016).

Fasano, G., & Franceschini, A. 1987, MNRAS, 225, 155
 Ferreira, J. 1997, A&A, 319, 340
 Filippenko, A. V. 1985, ApJ, 289, 475
 Filippenko, A. V., & Halpern, J. P. 1984, ApJ, 285, 458
 Fukumura, K., Tombesi, F., Kazanas, D., Shrader, C., Behar, E., & Contopoulos, I. 2014, ApJ, 780, 120
 Ganguly, R., Brotherton, M. S., Cales, S., Scoggins, B., Shang, Z., & Vestergaard, M. 2007, ApJ, 665, 990
 Glazebrook, K., Offer, A. R., & Deeley, K. 1998, ApJ, 492, 98
 Granato, G. L., De Zotti, G., Silva, L., Bressan, A., & Danese, L. 2004, ApJ, 600, 580
 Greene, J. E., & Ho, L. C. 2005, ApJ, 630, 122

Guillard, P., et al. 2012, ApJ, 747, 95
 Haehnelt, M. G., Natarajan, P., Rees, M. J. 1998, MNRAS, 300, 817
 Hagino, K., Odaka, H., Done, C., Gandhi, P., Watanabe, S., Sako, M., & Takahashi, T. 2015, MNRAS, 446, 663
 Hamann, F., & Sabra, B. 2004, AGN Physics with the Sloan Digital Sky Survey, Proceedings of a conference held in Princeton, NJ, USA, 27-31 July 2003, Edited by Gordon T. Richards and Patrick B. Hall, ASP Conference Series, Volume 311. San Francisco: Astronomical Society of the Pacific, 203
 Harrison, C. M., Alexander, D. M., Mullaney, J. R., & Swinbank, A. M. 2014, MNRAS, 441, 3306

- Heckman, T. M., & Best, P. N. 2014, *ARA&A*, 52, 589
- Heckman, T. M., & Kauffmann, G. 2006, *NewAR*, 50, 677
- Heckman, T. M., Miley, G. K., & Green, R. F. 1984, *ApJ*, 281, 525
- Heckman, T. M., Miley, G. K., van Breugel, W. J. M., & Butcher, H. R. 1981, *ApJ*, 247, 403
- Higginbottom, N., Proga, D., Knigge, C., Long, K. S., Matthews, J. H., & Sim, S. A. 2014, *ApJ*, 789, 19
- Hirschmann, M., Dolag, K., Saro, A., Borgani, S., & Burkert, A. 2014, *MNRAS*, 442, 2304
- Holt, J., Tadhunter, C. N., & Morganti, R. 2008, *MNRAS*, 387, 639
- Holt, J., Tadhunter, C. N., Morganti, R., & Emonts, B. H. C. 2011, *MNRAS*, 410, 1527
- Hopkins, P. F., Bundy, K., Hernquist, L., & Ellis, R. S. 2007, *ApJ*, 659, 976
- Hopkins, P. F., Cox, T. J., Keres, D., & Hernquist, L. 2008, *ApJS*, 175, 390
- Hu, C., Wang, J. M., Ho, L. C., et al. 2008, *ApJ*, 687, 78
- Ishibashi, W., & Fabian, A. C. 2014, *MNRAS*, 441, 1474
- Ishibashi, W., Fabian, A.C., & Canning, R.E.A. 2013, *MNRAS*, 431, 2350
- Kauffmann, G., & Haehnelt, M. 2000, *MNRAS*, 311, 576
- Kaspi, S., Maoz, D., Netzer, H., Peterson, B. M., Vestergaard, M., & Jannuzi, B. T. 2005, *ApJ*, 629, 61
- Kaspi, S., Smith, P.S., Netzer, H., Maoz, D., Jannuzi, B.T., & Giveon, U. 2000, *ApJ*533, 631
- Ker, L. M., Best, P. N., Rigby, E. E., Rttgering, H. J. A., & Gendre, M. A. 2012, *MNRAS*, 420, 2644
- Khalatyan, A., Cattaneo, A., Schramm, M., Gottlber, S., Steinmetz, M., & Wisotzki, L. 2008, *MNRAS*, 387, 13
- King, A. 2003, *ApJ*, 596, 27
- King, A. 2005, *ApJ*, 635, 121
- King, A. R., & Pounds, K. A. 2003, *MNRAS*, 345, 657
- Komossa, S., Xu, D., Zhou, H., Storchi-Bergmann, T., & Binette, L. 2008, *ApJ*, 680, 926
- Kormendy, J. & Ho, L. C. 2013, *ARA&A*, 51, 511
- Kriss, G. 1994, *Adass*, 3, 43
- Krolik, J. H., & Kriss, G. A. 2001, *ApJ*, 561, 684
- Laor, A., & Brandt, W. N. 2002, *ApJ*, 569, 461
- Liu, G. L., Zakamska, N. L.; Greene, J. E., Nesvadba, N. P. H., & Liu, X. 2013, *MNRAS*, 436, 2576
- Mahony, E. K., Morganti, R., Emonts, B. H. C., Oosterloo, T. A., & Tadhunter, C. 2013, *MNRAS*, 435, L58
- Maiolino, R., Gallerani, S., Neri, R., et al. 2012, *MNRAS*, 425, L66
- Malkan, M. A., & Sargent, W. L. W. 1982, *ApJ*, 254, 22
- Marconi, A., Axon, D. J., Maiolino, R., et al. 2008, *ApJ*, 678, 693
- Marziani, P., & Sulentic, J. W. 2012, *NewAR*, 56, 49
- Marziani, P., Sulentic, J. W., Zamanov, R., et al. 2003, *ApJS*, 145, 199
- Matsuoka, Y. 2012, *ApJ*, 2012, 750, 54
- Menci, N., Fiore, F., Puccetti, S., & Cavaliere, A. 2008, *ApJ*, 686, 219
- Morganti, R., Holt, J., Saripalli, L., Oosterloo, T. A., & Tadhunter, C. N. 2007, *A&A*, 476, 735
- Mullaney, J. R., Alexander, D. M., Fine, S., Goulding, A. D., Harrison, C. M., & Hickox, R. C. 2013, *MNRAS*, 433, 622
- Murray, N., Chiang, J., Grossman, S. A., & Voit, G. M. 1995, *ApJ*, 451, 498
- Nesvadba, N. P. H., Lehnert, M. D., De Breuck, C., Gilbert, A. M., & van Breugel, W. 2008, *A&A*, 491, 407
- Nesvadba, N. P. H., Lehnert, M. D., Eisenhauer, F., Gilbert, A., Tecza, M., & Abuter, R. 2006, *ApJ*, 650, 693
- Nomura, M., Ohsuga, K., Wada, K., Susa, H., & Misawa, T. 2013, *PASJ*, 65, 40
- Page, M. J., Symeonidis, M., Vieira, J. D., et al. *Nature*, 485, 213
- Panessa, F., et al. 2006, *A&A*, 455, 173
- Peacock, J. A. 1983, *MNRAS*, 202, 615
- Peterson, B. M. 2014, *SSRv*, 183, 253
- Peterson, B. M., & Bentz, M. C. 2006, *NewAR*, 50, 769
- Peterson, B. M., Ferrarese, L., Gilbert, K. M., Kaspi, S., Malkan, M. A., Maoz, D., Merritt, D., et al. 2004, *ApJ*, 613, 682
- Perez-Montero, E., & Diaz, A. I. 2003, *MNRAS*, 346, 105
- Pounds, K. A., King, A. R., Page, K. L., & O'Brien, P. T. 2003, *MNRAS*, 346, 1025
- Proga, D., & Kallman, T. R. 2004, *ApJ*, 616, 688
- Proga, D. 2003, *ApJ*, 585, 406
- Proga, D., Ostriker, J. P., & Kurosawa, R. 2008, *ApJ*, 676, 101
- Proga, D., Stone, J. M., & Drew, J. E. 1998, *MNRAS*, 295, 595
- Proga, D., Stone, J. M., & Kallman, T. R. 2000, *ApJ*, 543, 686
- Reeves, J. N., Sambruna, R. M., Braitto, V., & Eracleous, M. 2009, *ApJL*, 702, 187
- Rosario, D. J., Shields, G. A., Taylor, G. B., Salvander, S., & Smith, K. L. 2010, *ApJ*, 716, 131
- Schlegel, D., Finkbeiner, D. P., & Davies, M. 1998, *ApJ*, 500, 525
- Shen, Y., & Ho, Luis C. 2014, *Nature*, 513, 210
- Silk, J., & Rees, M. J. 1998, *A&A*, 331, L1
- Somerville, R. S., Hopkins, P. F., Cox, T. J., Robertson, B. E., & Hernquist, L. 2008, *MNRAS*, 391, 481
- Springel, V., White, S. D. M., Jenkins, A., et al. 2005, *Nature*, 435, 629

- Stepanovs, D., & Fendt, C. 2014, *ApJ*, 793, 31
- Storey, P. J., & Hummer, D. G. 1995, *MNRAS*, 272, 41
- Tombesi, F., Cappi, M., Reeves, J. N., & Braito, V. 2012, *MNRAS*, 422, L1
- Veron, P., Goncalves, A. C., & Veron-Cetty, M. -P. 2002, *A&A*, 384, 826
- Veron-Cetty, M.-P., Joly, M., & Veron, P. 2004, *A&A*, 417, 515
- Veron-Cetty, M.-P., Veron, P., & Goncalves, A. C. 2001, *A&A*, 372, 730
- Veilleux, S. 1991, *ApJS*, 75, 357
- Veilleux, S., Cecil, G., & Bland-Hawthorn, J. 20015, *ARA&A*, 43, 769
- Vestergaard, M., & Peterson, B. M. 2006, *ApJ*, 641, 689
- Villar-Martín, M., Arribas, S., Emonts, B., Humphrey, A., Tadhunter, C., Bessiere, P., Cabrera Lavers, A., & Ramos Almeida, C. 2016, *MNRAS*, 460, 130
- Wang, J. 2015, *NewA*, 37, 15
- Wang, J. M., Du, P., Hu, C., et al. 2014, *ApJ*, 793, 108
- Wang, J., Mao, Y. F., & Wei, J. Y. 2011, *ApJ*, 741, 50
- Wang, J., & Xu, D. W. 2015, *A&A*, 573, 15
- Wang, J., Xu, D. W., & Wei, J. Y. 2016, *AJ*, 151, 81
- Whittle, M. 1985, *MNRAS*, 213, 33
- Whittle, M., & Wilson, A.S. 2004. *AJ*, 127, 606
- Woo, J. H., Son, D., & Bae, H. J. 2017, *ApJ*, 839, 120
- Woo, J. H., & Urry, C. M. 2002, *ApJ*, 579, 530
- Wu, X. B., Wang, R., Kong, M. Z., Liu, F. K., & Han, J. L. 2004, *A&A*, 424, 793
- Xu, D. W., & Komossa, S. 2009, *ApJ*, 705, 20
- Zakamska, N. L., & Greene, J. E. 2014, *MNRAS*, 442, 784
- Zamanov, R., Marziani, P., Sulentic, J. W., et al. 2002, *ApJ*, 576, 9
- Zhang, K., Dong, X., Wang, T., & Gaskell, C. M. 2011, *ApJ*, 737, 71
- Zhang, K., Wang, T., Gaskell, C. M., & Dong, X. 2013, *ApJ*, 762, 51
- Zhou, H. Y., Wang, T. G., Yuan, W. M., Lu, H. L., Dong, X. B., Wang, J. X., & Lu, Y. J. 2006, *ApJS*, 166, 128
- Zubovas, K., & King, A. R. 2012, *MNRAS*, 426, 2751
- Zubovas, K., Nayakshin, S., King, A., & Wilkinson, M. 2013, *MNRAS*, 433, 3079